THE JOURNAL OF PHYSICAL CHEMISTRY C

Article

pubs.acs.org/JPCC

Atomic Structural Evolution during the Reduction of α-Fe_2O_3 Nanowires

Wenhui Zhu,[†] Jonathan Winterstein,[‡] Itai Maimon,[§] Qiyue Yin,[†] Lu Yuan,[†] Aleksey N. Kolmogorov,[§] Renu Sharma,[*,‡] and Guangwen Zhou[*,†]

[†]Department of Mechanical Engineering & Materials Science and Engineering Program, State University of New York, Binghamton, New York 13902, United States

[‡]Center for Nanoscale Science and Technology, National Institute of Standards and Technology, Gaithersburg, Maryland 20899, United States

[§]Department of Physics, State University of New York, Binghamton, New York 13902, United States

ABSTRACT: The atomic-scale reduction mechanism of α-Fe_2O_3 nanowires by H_2 was followed using transmission electron microscopy to reveal the evolution of atomic structures and the associated transformation pathways for different iron oxides. The reduction commences with the generation of oxygen vacancies that order onto every 10th $(30\bar{3}0)$ plane. This vacancy ordering is followed by an allotropic transformation of α-Fe_2O_3 → γ-Fe_2O_3 along with the formation of Fe_3O_4 nanoparticles on the surface of the γ-Fe_2O_3 nanowire by a topotactic transformation process, which shows 3D correspondence between the structures of the product and its host. These observations demonstrate that the partial reduction of α-Fe_2O_3 nanowires results in the formation of a unique hierarchical structure of hybrid oxides consisting of the parent oxide phase, γ-Fe_2O_3, as the one-dimensional wire and the Fe_3O_4 in the form of nanoparticles decorated on the parent oxide skeleton. We show that the proposed mechanism is consistent with previously published and our density functional theory results on the thermodynamics of surface termination and oxygen vacancy formation in α-Fe_2O_3. Compared to previous reports of α-Fe_2O_3 directly transformed to Fe_3O_4, our work provides a more in-depth understanding with substeps of reduction, i.e., the whole reduction process follows: α-Fe_2O_3 → α-Fe_2O_3 superlattice → γ-Fe_2O_3 + Fe_3O_4 → Fe_3O_4.

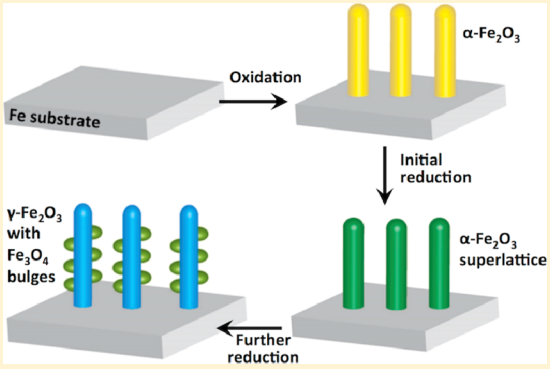

1. INTRODUCTION

Reduction treatment of metal oxides has been widely used to yield active materials for a large variety of applications ranging from catalysis to electronic devices.[1−5] For instance, metal oxides are used in heterogeneous catalysis as active catalysts, catalyst supports, and promoters. Reduced oxides are also used in electronic devices, magnetic memory, and as active/passive solar energy conversion materials.[6−8] The chemical and physical properties of metal oxides are crucially affected by their stoichiometry, phase, microstructure, atomic termination, and defects, all of which can be modified by a choice of reduction treatment. A fundamental understanding of the microscopic mechanism of the reduction of metal oxides is indispensable for obtaining controllable functionalities of the oxide.

Iron oxide, in particular, has many different phases, with Fe in variable oxidation states, depending upon the reduction process. The iron oxides include hematite (α-Fe_2O_3), magnetite (Fe_3O_4), and wustite (FeO). Fe_2O_3 exhibits various polymorphs including α-Fe_2O_3 (rhombohedral), γ-Fe_2O_3 (cubic), β-Fe_2O_3 (cubic), and ε-Fe_2O_3 (orthorhombic), among which α-Fe_2O_3 is the most thermodynamically stable phase (Figure 1a). Both γ-Fe_2O_3 (space group: $P4_132$, a = b = c = 0.8347 nm) and Fe_3O_4 (space group: $Fd\bar{3}m$, $a = b = c = 0.8394$ nm) share the cubic structure with close-packed oxygen atoms along the <111> direction but vary in the oxidation state for Fe (Figure 1b,c).[9,10] Magnetite contains both Fe^{2+} and Fe^{3+} ions in the crystal lattice and is sometimes formulated as $FeO{\cdot}Fe_2O_3$. In the crystal structure of Fe_3O_4, half of the Fe^{3+} ions are located in the tetrahedral interstitial sites, and the other half of the Fe^{3+} ions and all the Fe^{2+} ions occupy the octahedral sites (Figure 1c).[11] In γ-Fe_2O_3, due to the absence of Fe^{2+}, some of the Fe positions are left unoccupied as random vacancies (Figure 1b). FeO adopts the cubic, rock-salt structure, where Fe^{2+} ions are octahedrally coordinated by O^{2-} ions (Figure 1d). The applications for iron oxides intimately depend on their ability to redox (reduction and oxidation) cycle between the +2 and +3 oxidation states. However, the variable oxidation states of iron lead to a fairly complicated phase diagram of iron oxides with several easily interchangeable phases. Understanding the process of Fe_2O_3 reduction has therefore been a longstanding challenge.

Received: February 27, 2016
Revised: June 17, 2016
Published: June 20, 2016

DOI: 10.1021/acs.jpcc.6b02033
J. Phys. Chem. C 2016, 120, 14854−14862

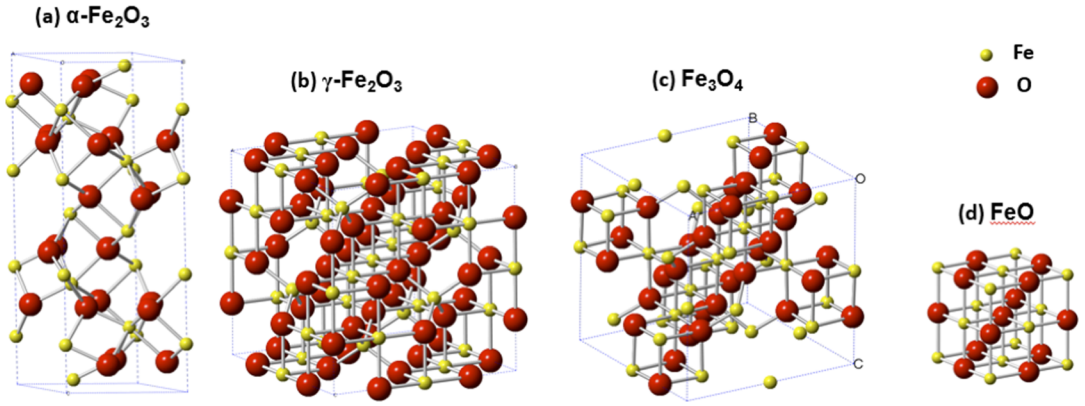

Figure 1. Crystallographic unit cell of different iron oxides: (a) α-Fe_2O_3, (b) γ-Fe_2O_3, (c) Fe_3O_4, and (d) FeO.

The reduction mechanism of iron oxides by hydrogen has been studied by macroscopically averaging approaches such as temperature-programmed reduction (TPR)[12] and X-ray diffraction.[13] Based on the TPR studies, two mechanisms have been proposed: a three-step mechanism, $Fe_2O_3 \rightarrow Fe_3O_4 \rightarrow FeO \rightarrow Fe$; and a two-step mechanism, $Fe_2O_3 \rightarrow Fe_3O_4 \rightarrow Fe$. While the reduction of a metal oxide usually commences via the nucleation and growth of a lower oxide as lattice oxygen escapes the parent phase, the microscopic process leading to the onset of the oxide reduction and the associated atomic structure evolution cannot be addressed using ensemble-averaging macroscopic approaches. Therefore, the aforementioned reduction pathways of Fe_2O_3 do not describe any polymorphic transition which might occur. In addition, the materials undergo crystallographic structural transformations and a full description of the process requires both the chemical composition and crystallographic information. Moreover, there is a lack of direct observation and careful study of the kinetic pathways of the oxide reduction at the atomic scale.

Nanostructured iron oxides, such as nanoparticles, nanowires, nanoblades, and nanorods, have drawn extensive research focus due to their great potential for broad applications, ranging from catalysis to drug delivery.[14,15] Previous reports about the reduction mechanism have primarily relied on observations of bulk materials. At the nanoscale, due to the size effect, different reduction behavior compared with the bulk might be anticipated. The nanowire is thus an ideal candidate, comprising a highly orientated skeleton, for studying how oxide reduction-induced phase transformations take place in one-dimensional systems.

Herein, we report the reaction pathway of H_2 induced reduction of α-Fe_2O_3 nanowires, using transmission electron microscopy (TEM) to reveal the atomic structure evolution in the oxide. We choose α-Fe_2O_3 because it has the most stable phase with highest oxidation state of Fe and can be employed as a model system to study the reaction pathway of oxide reduction. We identify the atomic process leading to crystal structure changes as the oxide is reduced from a higher oxidation state into lower ones. Particularly, we use α-Fe_2O_3 nanowires because the one-dimensional morphology is a highly anisotropic structure, making it simple to understand how reduction-induced physical transformations take place. We find the proposed mechanism to be consistent with previously published and our density functional theory (DFT) results on the thermodynamics of surface termination and oxygen vacancy formation in α-Fe_2O_3.

2. EXPERIMENTAL AND COMPUTATIONAL DETAILS

The α-Fe_2O_3 samples used for the reduction experiments were prepared using the thermal oxidation of polycrystalline Fe foils (99.99% purity). The high-purity Fe foils were first thoroughly rinsed in deionized water followed by ultrasonication in acetone for 5 min. The cleaned iron foils were then placed on a substrate heater in a vacuum chamber and the sample temperature was monitored by a K-type thermocouple in contact with the substrate heater. The chamber was pumped to vacuum ($\approx 3 \times 10^{-4}$ Pa) and then filled with oxygen gas at a pressure of ≈270 Pa (99.999% purity). The chamber was then sealed and the Fe sample was heated to the desired temperature (600 °C) at ≈20 °C min^{-1} in oxygen for 60 min. This yielded well-aligned, crystalline α-Fe_2O_3 nanowires perpendicular to the Fe substrate.[16−19] After the oxidation, the oxygen was pumped out, and the chamber was evacuated to $\sim 3 \times 10^{-4}$ Pa again. Subsequently, pure hydrogen gas (99.999% purity) at a pressure of ~270 Pa was admitted to the vacuum chamber. Meanwhile the temperature is reduced to 500 °C. After a reduction of 60 min at 500 °C in H_2, the Fe sample was cooled down in the same hydrogen atmosphere to room temperature at a rate of ~10 °C min^{-1}.

The morphologies of the α-Fe_2O_3 nanowires both before and after the H_2 reduction were examined using a field-emission scanning electron microscope (FEG-SEM). The atomic structures of the reduced nanowires were further analyzed using TEM operated at 200 kV. Electron energy-loss spectra (EELS), obtained with a monochromated electron source in the scanning transmission electron microscope (STEM), collected from reduced α-Fe_2O_3 nanowires were compared with those collected from four standard iron oxide samples (α-Fe_2O_3, γ-Fe_2O_3, Fe_3O_4, and FeO) under identical instrumental conditions, to measure the oxidation state of Fe at different reduction stages.

DFT calculations were performed with VASP[20,21] using the projector-augmented wave method[22] and the gradient-corrected Perdew, Burke and Ernzerhof (PBE)[23] exchange-correlation functional. Strong correlation effects were treated within the DFT+U approach[23,24] with a U = 4 eV value found to be suitable for Fe_2O_3 in previous studies.[25,26] For direct comparison, we adopted the default settings from the work by Souvi et al.[26] for the energy cutoff (600 eV), k-point meshes (7 × 7 × 3 in bulk and 7 × 7 × 1 in slab structures), and the size of the slab cell (a 3 nm c-axis). Atomic forces in local conjugate-gradient optimizations were reduced below 0.3 eV/nm, while the lattice constants were kept fixed at the experimental values

DOI: 10.1021/acs.jpcc.6b02033
J. Phys. Chem. C 2016, 120, 14854−14862

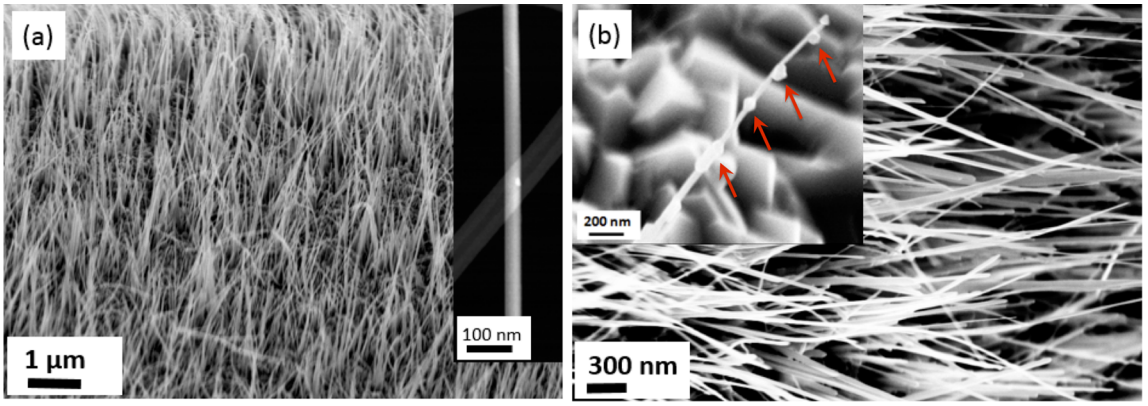

Figure 2. (a) SEM images of α-Fe_2O_3 nanowires formed from the oxidation of an Fe substrate; the inset is a STEM image of a single α-Fe_2O_3 nanowire revealing a smooth surface and uniform diameter. (b) SEM image of nanowires after reduction at 500 °C and 270 Pa of H_2 pressure for 50 min; the inset is a higher magnification SEM image showing the formation of bulges on the surface of the nanowires.

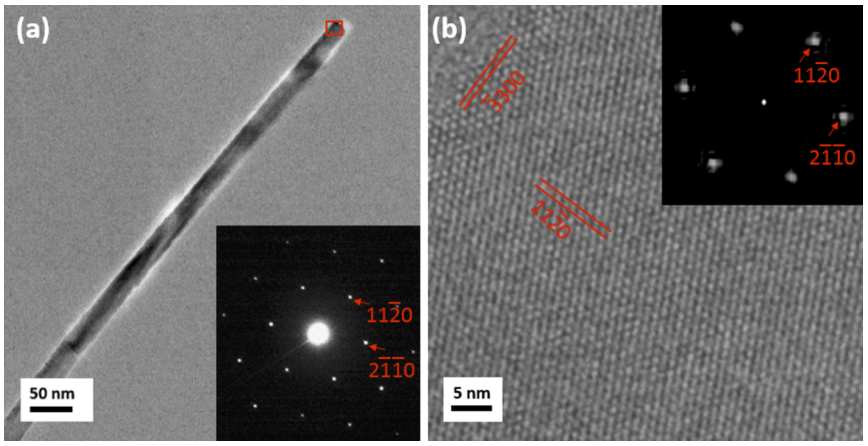

Figure 3. (a) TEM image of an α-Fe_2O_3 nanowire before the reduction treatment, the inset is a nanodiffraction pattern taken from the region indicated by the red box, revealing the [0001] zone axis of α-Fe_2O_3; (b) Representative HRTEM image obtained from the α-Fe_2O_3 nanowire in the area marked by the red box shown in panel a, revealing the perfect lattice structure in the unreduced nanowires. The inset is a diffractogram (fast Fourier transform) of the HRTEM image. The surface plane of the nanowire is $(\bar{3}300)$.

of a = 0.5035 nm (for bulk and slab structures) and c = 1.3747 nm (for bulk). We have reproduced and used the most stable antiferromagnetic arrangement on Fe^{3+} ions in bulk and slab calculations. Standard molecular dynamics (MD) runs were performed for slabs with 1 fs steps, a 400 eV energy cutoff, and a 5 × 5 × 1 k-mesh.

3. RESULTS AND DISCUSSION

Figure 2 shows the morphologies of α-Fe_2O_3 nanowires before and after the reduction. Figure 2a is a representative FEG-SEM image of the α-Fe_2O_3 nanowires as-prepared by the oxidation of a Fe foil. The densely distributed α-Fe_2O_3 nanowires are approximately perpendicular to the iron substrate and have lengths up to 5 μm with a relatively uniform diameter of about 50 nm. The inset in Figure 2a is a STEM image of a single α-Fe_2O_3 nanowire, showing that the nanowires have smooth surfaces. Although there is no significant change in the density and length of the nanowires after exposure to H_2 at 500 °C for 60 min, some nanowires developed a sawtooth surface morphology after the reduction reaction (Figure 2b). As revealed by the higher magnification FEG-SEM image (inset in Figure 2b), the surface of these sawtoothed nanowires is decorated with nanoparticles that are apparently formed during the H_2 reduction process. It should be also noted that a large fraction of the nanowires (≈ 60%, based on SEM image analysis of the reduced nanowires) still retain a smooth surface morphology, i.e., without the formation of nanoparticles on the parent nanowires. Among these nanowires with smooth surface morphology, some of them are still unreduced α-Fe_2O_3, indicating that the reduction is not uniform. This may relate to the stochastic population of defects in some nanowires, making them more reactive and easier to reduce compared with those without or with less defects.

Figure 3a shows a TEM image of the typical morphology of a single α-Fe_2O_3 nanowire before the reduction. Inset is a nanodiffraction pattern obtained from the nanowire, which can be indexed as α-Fe_2O_3 [0001]. Figure 3b is a representative high-resolution TEM (HRTEM) image from the α-Fe_2O_3 nanowire shown in Figure 3a and the upper-right inset is a diffractogram of the HRTEM image, which is consistent with the nanodiffraction pattern shown in Figure 3a. The surface plane is $(\bar{3}300)$, which is perpendicular to the $(11\bar{2}0)$. Both the diffraction pattern and high-resolution images confirm that the nanowires before reduction are α-Fe_2O_3.

Nanowires after reduction have two different morphologies: smooth and sawtoothed as shown in Figure 2b. The reduced nanowires with smooth morphology show minimal variation in diameter along the axial direction, i.e., no apparent bulge

DOI: 10.1021/acs.jpcc.6b02033
J. Phys. Chem. C 2016, 120, 14854−14862

formation on the surface (Figure 4a). However, superlattice diffraction spots can be seen in the ⟨30$\bar{3}$0⟩ direction of the α-Fe_2O_3, oriented along the [0001] zone axis, from the electron nanodiffraction pattern (Figure 4b). While defects are not immediately obvious upon the visual inspection of the HRTEM image of this nanowire ((Figure 4d), the corresponding diffractogram (upper-right inset of Figure 4b) shows the presence of superlattice spots, consistent with the diffraction pattern shown in Figure 4b. The result is different from the diffractogram obtained from the unreduced nanowires, where no superlattice reflections are present (inset of Figure 3b). In both the electron nanodiffraction and the diffractogram images, the fundamental spots are consistent with α-Fe_2O_3 [0001], indicating no change in the parent crystal structure.

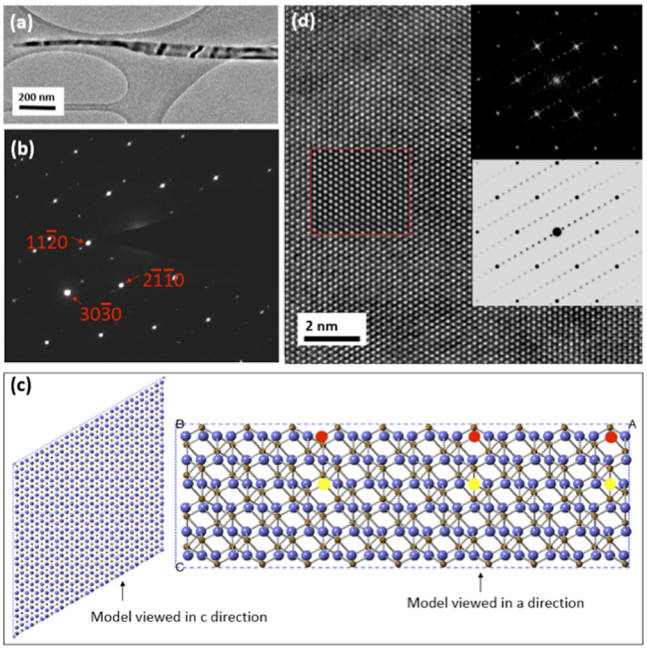

Figure 4. (a) TEM image showing the morphology of a reduced nanowire. (b) Nanodiffraction pattern of the nanowire along the α-Fe_2O_3 [0001] zone axis with extra spots along the [30$\bar{3}$0] direction. (c) Superstructure model, viewed in the *c*-direction and *a*-direction, built using 10 × 10 × 1 unit cell of the original α-Fe_2O_3 with oxygen vacancies marked by red or yellow circles. (d) HRTEM image of the α-Fe_2O_3 nanowire along the [0001] direction; the upper inset shows the diffractogram of the HRTEM image and the lower inset shows a simulated diffractogram based on the structure model shown in (c). The area within the red square is the simulated HRTEM image with a thickness of 18 nm and defocus value of −20 nm. The simulated HRTEM images are identical whether the lattice planes with the ordered oxygen vacancies are removed or placed in the superstructure, i.e., the vacancy ordering is not revealed in the simulated or the HRTEM images when viewed along the *c*-direction but it is apparent from the diffraction pattern and diffractogram.

The *d*-spacing between the adjacent spots in the superlattice direction is 1.45 nm, which is 10 times the *d*-spacing of the (30$\bar{3}$0) planes. The extra spots are parallel to the (30$\bar{3}$0) planes. The presence of superlattice reflections in the diffraction pattern and the diffractogram provide evidence that the reduction of the oxide is initiated by the formation of oxygen vacancies that self-order by condensing onto every 10th (30$\bar{3}$0) plane while the nanowires still maintain the crystalline structure of α-Fe_2O_3. Based on this information, we built a superstructure model using 10 × 10 × 1 unit cell of the original α-Fe_2O_3 with oxygen vacancies marked by red or yellow circles in Figure 4c. Structure models with different extents of reduction, i.e., different numbers of oxygen vacancies in the 10 × 10 × 1 supercell, were generated to simulate electron diffraction pattern and high-resolution images. The simulated HRTEM image (inset marked by red square in Figure 4d) with one layer of oxygen vacancies in the supercell matched well with the experimental one. Moreover, we found that the simulated images and diffraction patterns are dependent on the fraction of ordered vacancies in the superstructure model (extent of reduction). The best match is based on the model with 1/6 of every 10th (30$\bar{3}$0) plane's oxygen lattice site being occupied by a vacancy. That is, one of the six layers of oxygen in the supercell is occupied with the ordered vacancies, as shown in the view of the model from the "*a*" (lattice constant a) direction in Figure 4c. The observed partially reduced oxide nanowires, as shown in Figure 4, indicate that the oxide reduction is a multipathway process, most likely starting from the surface region, where the oxygen atoms are labile. Since reduction is a dynamic and continuous process, it is possible that the observed vacancy-ordering is just one of a series of ordering. We only observed the ordering of oxygen-vacancies on every 10th (30$\bar{3}$0) planes, which may be a relatively stable state and can be detected.

Vacancy migration is driven by the concentration gradient of oxygen vacancies. The concentration near the surface plane $\bar{3}$300 is higher than the core area of the nanowires because the oxygen atoms at the surface react first with hydrogen during reduction in H_2. We believe that the vacancy ordering is strain-induced because the strain could affect the formation energy of the oxygen vacancies.[27] We observed that most of the nanowires after reduction are bent due to the existence of strain. The strain affects the formation energy of oxygen vacancies. The formation of modulated structures induced by the long-range ordering of oxygen vacancies has also been observed in α-Fe_2O_3 nanowires produced by plasma oxidation of Fe[28,29] or electrical heating of Fe under ambient conditions[30] or treated in a reducing environment.[31] It was proposed that the existence of shear stress along the 30$\bar{3}$0 planes may be the driving force for the ordering of oxygen vacancies on the 30$\bar{3}$0 planes.[32] In addition, since the surface plane is ($\bar{3}$300), which is equivalent to (30$\bar{3}$0). They are in accordance because the vacancies initiated on $\bar{3}$300. As shown later, the superlattice structure induced by the long-range ordering of oxygen vacancies in the α-Fe_2O_3 nanowires is a metastable phase, which will be further reduced as the H_2 reduction continues.

In the TEM image (Figure 5a) of reduced nanowires with the sawtooth morphology (Figure 2b), a bulge is visible on the parent nanowire. Neither the electron diffraction pattern of the parent nanowire (area marked by circle b in Figure 5a) nor of the bulge area (circled area c in Figure 5a), as shown in Figure 5b,c, respectively, could be indexed as α-Fe_2O_3. However, both patterns can be indexed using either γ-Fe_2O_3 or Fe_3O_4 structures. Note that no superlattice is visible, meaning the ratio of Fe to O is no longer 2:3, i.e., some Fe^{3+} must have transformed to Fe^{2+}. The HRTEM image in Figure 5d is obtained from the interface area (marked by the square D in Figure 5a) between the parent nanowire and the bulge. It is clear that the lattice planes run continuously from the nanowire region to the bulge, i.e., there is no clear/sharp interface area between the bulge and the parent nanowire, which is in line with a previous report showing the formation of continuous

DOI: 10.1021/acs.jpcc.6b02033
J. Phys. Chem. C 2016, 120, 14854−14862

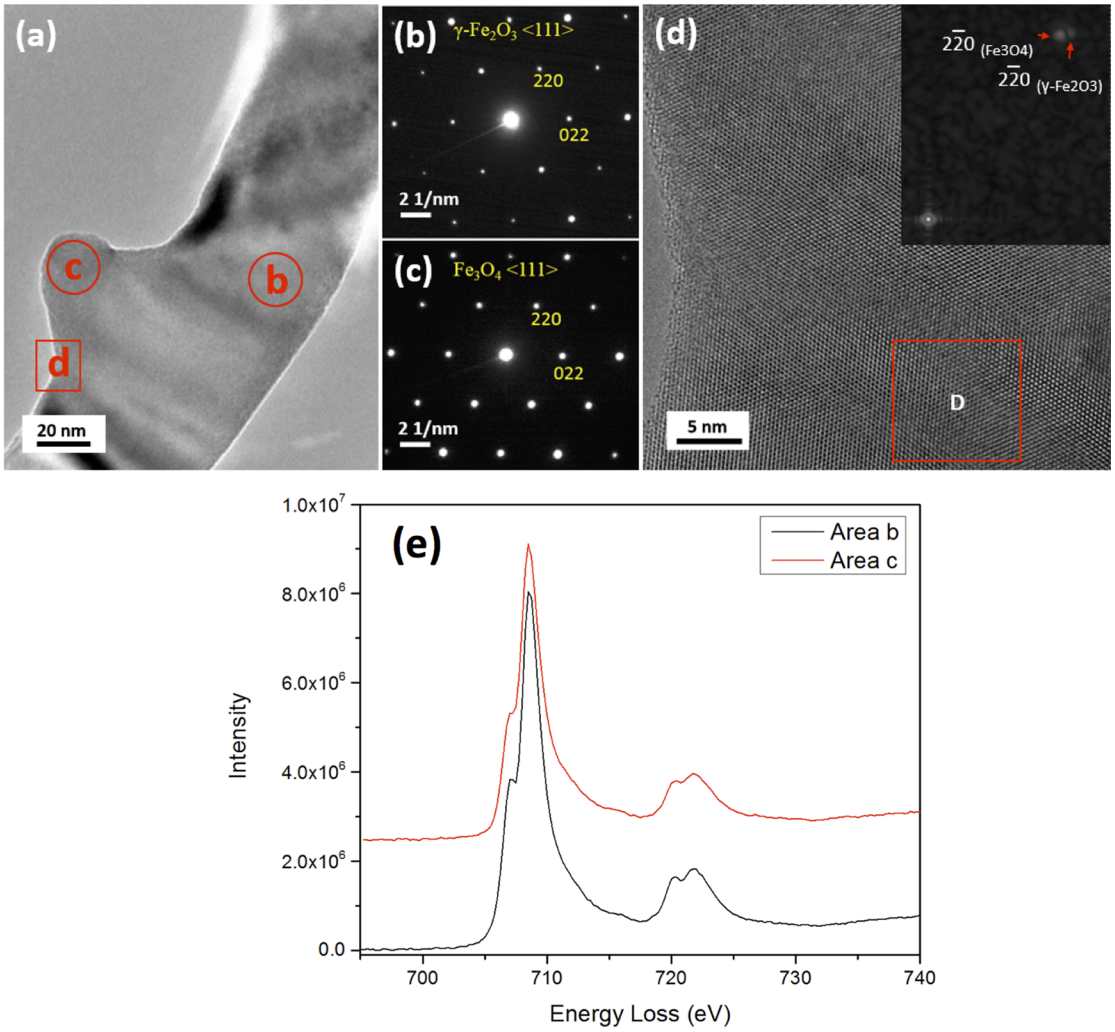

Figure 5. (a) TEM image of a reduced oxide nanowire with a bulge after further reduction. (b) Nanodiffraction pattern from the reduced nanowire (marked by the red circle 'b' in panel a). (c) Nanodiffraction pattern from the bulge region (marked by the red circle 'c' in panel a). (d) the HRTEM image recorded from the area marked by square d in panel a. The diffractogram shows two patterns that originate from the reduced nanowire and the bulge, respectively. (e) EELS from the reduced nanowire and the bulge regions, respectively. The spectra have been deconvoluted and aligned using the L_3 edge for comparison.

Table 1. L_3/L_2 Ratio of the Reduced Products of α-Fe_2O_3 Nanowires and the Standard Commercial Nanoparticles of Different Iron Oxides

iron oxides	α-Fe_2O_3	γ-Fe_2O_3	Fe_3O_4	FeO	reduced nanowire (area b in Figure 5a)	reduced nanowire bulge (area c in Figure 5a)
L_3/L_2 ratio of Fe L edge	5.23 ± 0.01	5.11 ± 0.01	4.61 ± 0.01	4.48 ± 0.01	5.20 ± 0.01	4.63 ± 0.01
oxidation state	3	3	2.67	2	3	2.67

lattice planes across the γ-Fe_2O_3/Fe_3O_4 interface.[33,34] However, the FFT pattern (inset in Figure 5d) from the area marked with square box D in Figure 5d on which the bulge has developed, shows two sets of diffraction patterns, which are the ⟨111⟩ of γ-Fe_2O_3 and Fe_3O_4.

It is challenging to distinguish γ-Fe_2O_3 and Fe_3O_4 structures by electron nanodiffraction because they have lattice constants within ~0.5% as mentioned before (Figure 1b,c). However, for 3d transition metals, the 3d states are partially filled, which allow the 2p core electrons to be excited into the unoccupied 3d-orbital represented by L_2 and L_3 lines (white lines) in EELS.[35,36] The intensity ratio of these white lines is therefore dependent upon the oxidation state of the metal. Since the Fe in the two phases have different oxidation states, the two phases can be distinguished by measuring the L_3/L_2 ratio in the EELS data collected from the parent and bulge regions of nanowires.

To do this, we first we prepared calibration standards using commercially available nanoparticle samples of different iron oxides, including α-Fe_2O_3, γ-Fe_2O_3, Fe_3O_4, and FeO. We analyzed them by STEM-EELS under the same conditions to compare the L_3/L_2 ratio. EELS spectra (Figure 5e) were acquired under identical conditions from the parent nanowire (marked with b in Figure 5a) and the bulge area (marked with c in Figure 5a). All the spectra were background-subtracted using power-law curve fitting, and were deconvoluted to minimize the size or thickness effects.[37,38] The L_3/L_2 ratios were calculated

DOI: 10.1021/acs.jpcc.6b02033
J. Phys. Chem. C 2016, 120, 14854−14862

by using two arctangent functions to remove the postedge backgrounds and to produce the isolated Fe L_3 and L_2 edges:[39] the results are listed in Table 1. The uncertainty is given by the standard deviation of multiple measurements. By comparing with the L_3/L_2 ratios of the standard samples of the iron oxides, we find that the values for the L_3/L_2 ratios from the reduced parent nanowire and the bulged region are close to those for Fe_2O_3 and Fe_3O_4, respectively.[33] Therefore, we conclude that the phase in Figure 5b is γ-Fe_2O_3 ⟨111⟩ and in Figure 5c is Fe_3O_4 ⟨111⟩. Both γ-Fe_2O_3 and Fe_3O_4 are thermodynamically metastable phases. The occurrence of γ-Fe_2O_3 as a transition phase to Fe_3O_4 is in accordance with kinetic considerations, i.e., the lower kinetic barrier for the transformation from α-Fe_2O_3 to γ-Fe_2O_3 than from α-Fe_2O_3 to Fe_3O_4 allows this phase transition to take place. This has also been observed during the oxidation of Fe particles.[40,41] Figure 6 illustrates schematically the pathway of the crystallographic transformation based on our experimental observations of the reduction of α-Fe_2O_3 nanowires. The reduction of the α-Fe_2O_3 nanowires, formed by oxidation of the Fe foil, as reported extensively in our previous work,[19,32,42,43] starts by the formation of random oxygen vacancies due to the removal of lattice oxygen by H_2. During continued reduction, oxygen vacancies order via vacancy coalescence on every 10th $(30\bar{3}0)$ plane that results in a partially reduced α-Fe_2O_3 nanowire with no morphological change. As the reduction continues, and more oxygen vacancies form; the α-Fe_2O_3 structure becomes unstable and transforms to the γ-Fe_2O_3/Fe_3O_4 hybrid structure. The loss of oxygen-vacancy ordering, which is evident by the disappearance of the extra spots in the diffraction pattern, is accompanied by the partial change of oxidation state of Fe, forming Fe_3O_4 as a bulge having a topotactic orientation relationship with the γ-Fe_2O_3 nanowire. The theoretical densities for α-Fe_2O_3 and γ-Fe_2O_3 are 5.27 g·cm^{-3} and 5.47 g·cm^{-3}, respectively. For the transformation of the parent nanowires from α-Fe_2O_3 to γ-Fe_2O_3, there is a volume shrinkage by ≈3%. As shown from our TEM observations, the shape of the nanowire remains relatively unchanged, suggesting there is little diffusion involved or needed for the phase transition. Moreover, there is only a small change in composition, still very close to an allotropic transformation. The long-range ordering of oxygen vacancies disappears after enabling the allotropic transformation in the nanowires.

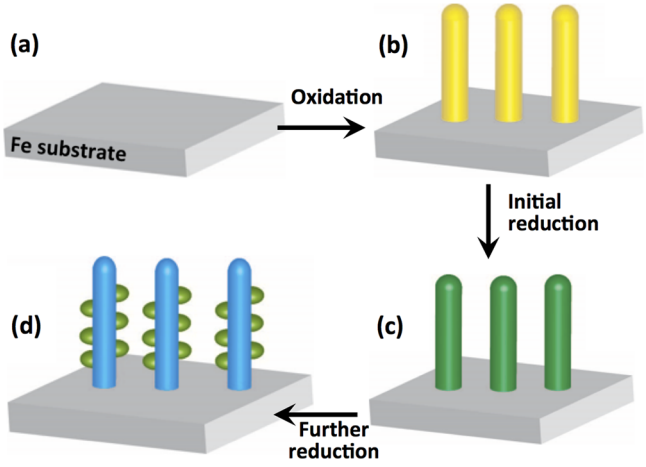

Figure 6. Illustration of the combined oxidation−reduction reactions that lead to the formation of the hybrid structure of iron oxides, (a) Fe substrate, (b) α-Fe_2O_3 nanowires grown on the Fe substrate, (c) α-Fe_2O_3 nanowires with the superlattice of oxygen vacancies, (d) γ-Fe_2O_3 nanowire with Fe_3O_4 bulges. There is slight volume shrinkage of the nanowires when transformed to γ-Fe_2O_3 nanowire with Fe_3O_4 bulges.

Although the γ-Fe_2O_3 and the Fe_3O_4, structures are very similar, their densities are different. The unit cell volume of γ-Fe_2O_3 is 0.5816 $(nm)^3$ and there are 12 formula units in the unit cell, i.e., the theoretical density is 5.47 g·cm^{-3}; while for Fe_3O_4, the unit cell volume is 0.5915 $(nm)^3$ with eight formula units in it, which gives a theoretical density of 5.10 g·cm^{-3}.[44] Therefore, the transformation from γ-Fe_2O_3 to Fe_3O_4 is accompanied by a volume expansion of ∼7%[9] and results in the formation of bulges on the parent nanowires.

It has been shown that hydroxyls (OH) can form on the hematite surface upon exposure to hydrogen at room temperature, which recombine to H_2O and then desorb upon heating to ∼275 K.[45] Because of the significantly higher temperature (∼800 K) employed in our reduction experiments, it is reasonable to expect that hydroxyls exist only as an intermediate and quickly desorb from the surface as H_2O molecules, which results in the reduction of α-Fe_2O_3. While full ab initio modeling of the reduction process is challenging, select steps can be checked qualitatively against previously published and present DFT results. A number of DFT studies have been dedicated to examination of hematite's bulk and surface properties.[20,25,26,46−48] Souvi et al. reported a detailed analysis of the α-Fe_2O_3 adsorption thermodynamics in the presence of O_2, H_2O, and H_2 gases.[26] Based on these findings, our samples exposed to O_2 under all considered (P, T) conditions most likely had purely Fe-terminated surfaces (Fe−O_3−Fe in Figure 7a). According to the calculated phase stability diagrams for hydrogenated surfaces,[26] one should expect different partial H coverages in the relevant (P, T) ranges. At 270 Pa and 900 K, the most stable configuration was found to be Fe−O_3−H−Fe, in which one out of the three topmost O atoms forms an OH group. At lower temperatures, a more H-rich Fe−O_3−2H−Fe configuration with a slightly reconstructed surface was determined to be thermodynamically stable, in which the formation of the second OH group pushed the O atom above the topmost Fe atom (see Figure 7b).

We performed several MD runs to obtain additional information on the behavior of the system in the H_2-rich environment at elevated temperatures. In order to accelerate the exploration of relevant nearby configurations in our longest simulation we set the temperature to the highest 800 K value used in the experiment. Starting with the previously reported stable Fe−O_3−2H−Fe structure,[26] we evolved the system for 10 ps (10 000 steps) and monitored relative positions of the atoms at one of the surfaces. Figure 7d demonstrates that among the three surface O atoms the two that are capped with H tend to stay above the average Fe position. This behavior can be attributed to a weaker bonding of the two H-capped O atoms with the subsurface Fe ions and to the configurational entropy factor that forces the system at high temperatures to stay predominantly in regions with abundance of nearly degenerate states. Figure 7e tracks the O−H distances and reveals several instances of the O atoms acquiring a second H neighbor. The relaxed structure extracted at 1.3 ps was found to have the second nearest O−H distance of 0.157 nm and to be a local minimum only 0.13 eV above the initial state (Figure 7c). Several structures appearing after 6.3 ps featured even shorter second O−H bond lengths as low as 0.120 nm. Despite not

DOI: 10.1021/acs.jpcc.6b02033
J. Phys. Chem. C 2016, 120, 14854−14862

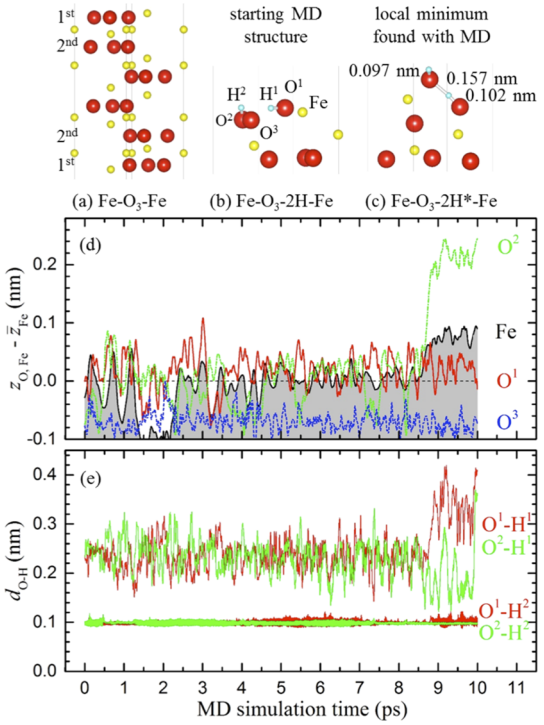

Figure 7. (a) A symmetric Fe-terminated slab of α-Fe_2O_3 used for DFT simulation of vacancies; the two O layers closest to the surface on both sides are labeled as 1st and 2nd. (b) The top part of a H-terminated slab structure found to be most stable in the work done by Souvi et al.[26] and used as a starting point in our MD runs. (c) The top part of a H-terminated slab structure identified in our MD simulation (at 1.3 ps) and relaxed with the conjugate-gradient algorithm. (d) z coordinates of O and Fe atoms shown in panel b above the average z coordinate of the Fe atom during the MD simulation. (e) O−H distances between surface atoms shown in panels b and c.

being local minima, configurations observed after 8.5 ps had one OH group consistently above the top Fe atom.

Although DFT-level MD simulations for systems of such size can rarely be used for determining or quantifying all relevant transformations, our results indicate that adsorbed H atoms show no propensity for migrating into the oxide but rather form H−OH complexes on the oxide's surface. These frequently appearing motifs at typical H reduction temperatures are still strongly bonded to the surface Fe and/or O atoms but could be viewed as water molecule precursors. Identification of all intermediate steps and transition paths determining the removal of water molecules from the surface and, consequently, creation of a surface O vacancy (V_O) will require a separately dedicated study. It will be interesting to compare the desorption paths and barriers to those obtained previously for select Fe- and O-terminated surfaces.[20]

Our last set of DFT calculations provides information on the energetics of creating V_O in different bulk and surface α-Fe_2O_3 structures. For quantifying the V_O−V_O and V_O−surface proximity effects, we calculated and compared V_O formation energies in 2 bulk and 4 slab configurations. As in our previous study of vacancies in CuO,[49] analysis of V_O formation energy differences at the same (P, T) conditions does not require (P, T)-dependent adjustment of the chemical potential for O_2 calculated at 0 K, as the correction cancels out. In the largest considered 2 × 2 × 1 bulk supercell, with vacancies separated by ∼1 nm laterally and ∼1.4 nm vertically, the 0-K defect formation energy was found to be 4.24 eV/V_O. A reduction by 0.25 eV/V_O was observed for the conventional 1 × 1 × 1unit cell (Figure 1a), in which a single vacancy site is surrounded by 6 nearest images ∼0.5 nm away in the x−y plane. The slab unit cell has the same lateral dimensions and we can isolate the influence of the surface by using the 3.99 eV/V_O value from the 1 × 1 × 1 bulk calculation as a reference. Removal of a single O atom in different (sub)surface O layers shown in Figure 7a resulted in lowering the V_O formation energy by 0.07 eV/V_O for the second layer and by 0.44 eV/V_O for the first one. It is worth noting that creation of vacancy pairs symmetrically in ether two first layers or two second layers on the opposite slab surfaces resulted in virtually identical defect energies per V_O, which is not surprising considering that the two second layers on the opposite sides are already 0.72 nm apart. The findings suggest that even for relatively small separations of about 0.5 nm the direct V_O−V_O interaction does not exceed 0.1 eV/V_O. Presence of the surface has a noticeable effect on the V_O formation energy only in the first O layer. In dynamic equilibrium at 800 K, the ∼0.4 eV/V_O difference would cause about a 100-fold difference in the vacancy concentration in the surface and bulk layers. In the considered process, the relative vacancy concentrations also depend on the kinetics factors defining the O removal rate from the surface and the O diffusion rate from bulk to surface.

4. CONCLUSION

In summary, we have shown that the reduction of metal oxide nanowires can be employed to generate hybrid oxides that combine the metal in different oxidation states. The reduction starts with the formation of an ordered lattice of oxygen vacancies, forming the partially reduced α-Fe_2O_3 superstructure. As reduction continues, the α-Fe_2O_3 nanowires transformed into a γ-Fe_2O_3/Fe_3O_4 hybrid structure. The resulting oxide composites consist of the transformed oxide phase (γ-Fe_2O_3) that remains as the skeleton and the lower oxides (Fe_3O_4) that have the form of nanoscale bulges decorating the transformed oxide skeleton. The mechanism underlying the formation of these unique hybrid oxides is identified as an allotropic transformation of α-Fe_2O_3 → γ-Fe_2O_3 via the annihilation of oxygen vacancies in the parent α-Fe_2O_3, which is followed by a topotactic transformation of the γ-Fe_2O_3 → Fe_3O_4 via the nucleation of Fe_3O_4 nanoparticles on the surface of the transformed γ-Fe_2O_3 nanowires. Our DFT results are consistent with the experimental ones. Compared to previous report of α-Fe_2O_3 directly reduced to Fe_3O_4, our work provides a more in-depth understanding with substeps of reduction, i.e, the superlattice formation by oxygen vacancy ordering and the allotropic transformation happened during α-Fe_2O_3 → Fe_3O_4. The whole reduction process follows: α-Fe_2O_3 → α-Fe_2O_3 superlattice → γ-Fe_2O_3 + Fe_3O_4 → Fe_3O_4.

AUTHOR INFORMATION

Corresponding Authors

*(R.S.) E-mail: renu.sharma@nist.gov; phone: 301-975-2418.
*(G.Z.) E-mail: gzhou@binghamton.edu; phone: 607-777-5084.

Notes

The authors declare no competing financial interest.

DOI: 10.1021/acs.jpcc.6b02033
J. Phys. Chem. C 2016, 120, 14854−14862

■ ACKNOWLEDGMENTS

This work was supported by the National Science Foundation under NSF CAREER Award Grant CMMI-1056611. I.M. and A.N.K. gratefully acknowledge the NSF support (Award No. DMR-1410514).

■ REFERENCES

(1) Prosini, P. P.; Carewska, M.; Loreti, S.; Minarini, C.; Passerini, S. Lithium Iron Oxide as Alternative Anode for Li-Ion Batteries. *Int. J. Inorg. Mater.* **2000**, *2*, 365−370.
(2) Siroky, K.; Jiresova, J.; Hudec, L. Iron-Oxide Thin-Film Gas Sensor. *Thin Solid Films* **1994**, *245*, 211−214.
(3) Hermanek, M.; Zboril, R.; Medrik, N.; Pechousek, J.; Gregor, C. Catalytic Efficiency of Iron(III) Oxides in Decomposition of Hydrogen Peroxide: Competition between the Surface Area and Crystallinity of Nanoparticles. *J. Am. Chem. Soc.* **2007**, *129*, 10929−10936.
(4) Carabineiro, S. A. C.; Bogdanchikova, N.; Tavares, P. B.; Figueiredo, J. L. Nanostructured Iron Oxide Catalysts with Gold for the Oxidation of Carbon Monoxide. *RSC Adv.* **2012**, *2*, 2957−2965.
(5) Abou Hassan, A.; Sandre, O.; Cabuil, V.; Tabeling, P. Synthesis of Iron Oxide Nanoparticles in a Microfluidic Device: Preliminary Results in a Coaxial Flow Millichannel. *Chem. Commun.* **2008**, 1783−1785.
(6) Klahr, B. M.; Martinson, A. B.; Hamann, T. W. Photoelectrochemical Investigation of Ultrathin Film Iron Oxide Solar Cells Prepared by Atomic Layer Deposition. *Langmuir* **2011**, *27*, 461−468.
(7) Mohr, R.; Kratz, K.; Weigel, T.; Lucka-Gabor, M.; Moneke, M.; Lendlein, A. Initiation of Shape-Memory Effect by Inductive Heating of Magnetic Nanoparticles in Thermoplastic Polymers. *Proc. Natl. Acad. Sci. U. S. A.* **2006**, *103*, 3540−3545.
(8) Miller, E. L.; Paluselli, D.; Marsen, B.; Rocheleau, R. E. Low-Temperature Reactively Sputtered Iron Oxide for Thin Film Devices. *Thin Solid Films* **2004**, *466*, 307−313.
(9) Wang, C. M.; Baer, D. R.; Amonette, J. E.; Engelhard, M. H.; Antony, J.; Qiang, Y. Morphology and Electronic Structure of the Oxide Shell on the Surface of Iron Nanoparticles. *J. Am. Chem. Soc.* **2009**, *131*, 8824−8832.
(10) Ding, Y.; Morber, J. R.; Snyder, R. L.; Wang, Z. L. Nanowire Structural Evolution from Fe_3O_4 to ε-Fe_2O_3. *Adv. Funct. Mater.* **2007**, *17*, 1172−1178.
(11) Zboril, R.; Mashlan, M.; Petridis, D. Iron(III) Oxides from Thermal Processes-Synthesis, Structural and Magnetic Properties, Mossbauer Spectroscopy Characterization, and Applications. *Chem. Mater.* **2002**, *14*, 969−982.
(12) Lin, H. Y.; Chen, Y. W.; Li, C. P. The Mechanism of Reduction of Iron Oxide by Hydrogen. *Thermochim. Acta* **2003**, *400*, 61−67.
(13) Zielinski, J.; Zglinicka, I.; Znak, L.; Kaszkur, Z. Reduction of Fe_2O_3 with Hydrogen. *Appl. Catal., A* **2010**, *381*, 191−196.
(14) Liu, P. J.; He, S. B.; Wei, H. Z.; Wang, J. H.; Sun, C. L. Characterization of α-Fe_2O_3/γ-Al_2O_3 Catalysts for Catalytic Wet Peroxide Oxidation of M-Cresol. *Ind. Eng. Chem. Res.* **2015**, *54*, 130−136.
(15) Gomez-Sotomayor, R.; Ahualli, S.; Viota, J. L.; Rudzka, K.; Delgado, A. V. Iron/Magnetite Nanoparticles as Magnetic Delivery Systems for Antitumor Drugs. *J. Nanosci. Nanotechnol.* **2015**, *15*, 3507−3514.
(16) Yuan, L.; Cai, R. S.; Jang, J. I.; Zhu, W. H.; Wang, C.; Wang, Y. Q.; Zhou, G. W. Morphological Transformation of Hematite Nanostructures During Oxidation of Iron. *Nanoscale* **2013**, *5*, 7581−7588.
(17) Yuan, L.; Jiang, Q. K.; Wang, J. B.; Zhou, G. W. The Growth of Hematite Nanobelts and Nanowires-Tune the Shape Via Oxygen Gas Pressure. *J. Mater. Res.* **2012**, *27*, 1014−1021.
(18) Yuan, L.; Wang, Y. Q.; Cai, R. S.; Jiang, Q. K.; Wang, J. B.; Li, B. Q.; Sharma, A.; Zhou, G. W. The Origin of Hematite Nanowire Growth During the Thermal Oxidation of Iron. *Mater. Sci. Eng., B* **2012**, *177*, 327−336.
(19) Yuan, L.; Wang, Y. Q.; Mema, R.; Zhou, G. W. Driving Force and Growth Mechanism for Spontaneous Oxide Nanowire Formation During the Thermal Oxidation of Metals. *Acta Mater.* **2011**, *59*, 2491−2500.
(20) Kresse, G.; Hafner, J. *Ab Initio* Molecular Dynamics for Liquid Metals. *Phys. Rev. B: Condens. Matter Mater. Phys.* **1993**, *47*, 558−561.
(21) Kresse, G.; Furthmüller, J. Efficient Iterative Schemes for *Ab Initio* Total-Energy Calculations Using a Plane-Wave Basis Set. *Phys. Rev. B: Condens. Matter Mater. Phys.* **1996**, *54*, 11169−11186.
(22) Perdew, J. P.; Burke, K.; Ernzerhof, M. Generalized Gradient Approximation Made Simple. *Phys. Rev. Lett.* **1996**, *77*, 3865−3868.
(23) Anisimov, V. I.; Zaanen, J.; Andersen, O. K. Band Theory and Mott Insulators: Hubbard *U* Instead of Stoner *I*. *Phys. Rev. B: Condens. Matter Mater. Phys.* **1991**, *44*, 943−954.
(24) Rollmann, G.; Rohrbach, A.; Entel, P.; Hafner, J. First-Principles Calculation of the Structure and Magnetic Phases of Hematite. *Phys. Rev. B: Condens. Matter Mater. Phys.* **2004**, *69*, 165107.
(25) Souvi, S. M. O.; Badawi, M.; Paul, J.-F.; Cristol, S.; Cantrel, L. A DFT Study of the Hematite Surface State in the Presence of H2, H2o and O2. *Surf. Sci.* **2013**, *610*, 7−15.
(26) Xiao, J.; Frauenheim, T. Activation Mechanism of Carbon Monoxide on A-Fe_2O_3 (0001) Surface Studied by Using First Principle Calculations. *Appl. Phys. Lett.* **2012**, *101*, 041603.
(27) Aschauer, U.; Pfenninger, R.; Selbach, S. M.; Grande, T.; Spaldin, N. A. Strain-Controlled Oxygen Vacancy Formation and Ordering in $Camno_3$. *Phys. Rev. B: Condens. Matter Mater. Phys.* **2013**, *88*, 054111.
(28) Chen, Z. Q.; Cvelbar, U.; Mozetic, M.; He, J. Q.; Sunkara, M. K. Long-Range Ordering of Oxygen-Vacancy Planes in α-Fe2O3 Nanowires and Nanobelts. *Chem. Mater.* **2008**, *20*, 3224−3228.
(29) Cvelbar, U.; Chen, Z. Q.; Sunkara, M. K.; Mozetic, M. Spontaneous Growth of Superstructure α-Fe_2O_3 Nanowire and Nanobelt Arrays in Reactive Oxygen Plasma. *Small* **2008**, *4*, 1610−1614.
(30) Nasibulin, A.; Rackauskas, S.; Jiang, H.; Tian, Y.; Mudimela, P.; Shandakov, S.; Nasibulina, L.; Jani, S.; Kauppinen, E. Simple and Rapid Synthesis of α-Fe_2O_3 Nanowires under Ambient Conditions. *Nano Res.* **2009**, *2*, 373−379.
(31) Lee, Y. C.; Chueh, Y. L.; Hsieh, C. H.; Chang, M. T.; Chou, L. J.; Wang, Z. L.; Lan, Y. W.; Chen, C. D.; Kurata, H.; Isoda, S. P-Type a-Fe_2O_3 Nanowires and Their n-Type Transition in a Reductive Ambient. *Small* **2007**, *3*, 1356−1361.
(32) Cai, R. S.; Li, T.; Wang, Y. Q.; Wang, C.; Yuan, L.; Zhou, G. W. Formation of Modulated Structures in Single-Crystalline Hexagonal α-Fe_2O_3 Nanowires. *J. Nanopart. Res.* **2012**, *14*, 1−11.
(33) Tang, J.; Myers, M.; Bosnick, K. A.; Brus, L. E. Magnetite Fe_3o_4 Nanocrystals: Spectroscopic Observation of Aqueous Oxidation Kinetics. *J. Phys. Chem. B* **2003**, *107*, 7501−7506.
(34) Zhu, W.; Winterstein, J. P.; Sharma, R.; Zhou, G. Atomic-Scale Characterization of the Reduction of a-Fe_2o_3 Nanowires. *Microsc. Microanal.* **2015**, *21*, 995−996.
(35) Schmid, H. K.; Mader, W. Oxidation States of Mn and Fe in Various Compound Oxide Systems. *Micron* **2006**, *37*, 426−432.
(36) Wang, Z. L.; Yin, J. S.; Jiang, Y. D. Eels Analysis of Cation Valence States and Oxygen Vacancies in Magnetic Oxides. *Micron* **2000**, *31*, 571−580.
(37) Verbeeck, J.; Van Aert, S. Model Based Quantification of Eels Spectra. *Ultramicroscopy* **2004**, *101*, 207−224.
(38) Tan, H.; Verbeeck, J.; Abakumov, A.; Van Tendeloo, G. Oxidation State and Chemical Shift Investigation in Transition Metal Oxides by Eels. *Ultramicroscopy* **2012**, *116*, 24−33.
(39) Cavé, L.; Al, T.; Loomer, D.; Cogswell, S.; Weaver, L. A Stem/Eels Method for Mapping Iron Valence Ratios in Oxide Minerals. *Micron* **2006**, *37*, 301−309.
(40) Cabot, A.; Puntes, V. F.; Shevchenko, E.; Yin, Y.; Balcells, L.; Marcus, M. A.; Hughes, S. M.; Alivisatos, A. P. Vacancy Coalescence During Oxidation of Iron Nanoparticles. *J. Am. Chem. Soc.* **2007**, *129*, 10358−10360.

DOI: 10.1021/acs.jpcc.6b02033
J. Phys. Chem. C 2016, 120, 14854−14862

(41) Signorini, L.; Pasquini, L.; Savini, L.; Carboni, R.; Boscherini, F.; Bonetti, E.; Giglia, A.; Pedio, M.; Mahne, N.; Nannarone, S. Size-Dependent Oxidation in Iron/Iron Oxide Core-Shell Nanoparticles. *Phys. Rev. B: Condens. Matter Mater. Phys.* **2003**, *68*, 195423.
(42) Yuan, L.; Wang, Y.; Cai, R.; Jiang, Q.; Wang, J.; Li, B.; Sharma, A.; Zhou, G. The Origin of Hematite Nanowire Growth During the Thermal Oxidation of Iron. *Mater. Sci. Eng., B* **2012**, *177*, 327−336.
(43) Yuan, L.; Jiang, Q.; Wang, J.; Zhou, G. The Growth of Hematite Nanobelts and Nanowires—Tune the Shape Via Oxygen Gas Pressure. *J. Mater. Res.* **2012**, *27*, 1014−1021.
(44) Levy, D.; Giustetto, R.; Hoser, A. Structure of Magnetite (Fe_3O_4) above the Curie Temperature: A Cation Ordering Study. *Phys. Chem. Miner.* **2012**, *39*, 169−176.
(45) Huang, W.; Ranke, W.; Schlögl, R. Reduction of an A-Fe_2o_3 (0001) Film Using Atomic Hydrogen. *J. Phys. Chem. C* **2007**, *111*, 2198−2204.
(46) Nguyen, M.-T.; Seriani, N.; Gebauer, R. Water Adsorption and Dissociation on α-Fe_2o_3(0001): PBE + U Calculations. *J. Chem. Phys.* **2013**, *138*, 194709.
(47) Wang, X. G.; Weiss, W.; Shaikhutdinov, S. K.; Ritter, M.; Petersen, M.; Wagner, F.; Schlögl, R.; Scheffler, M. The Hematite a-Fe_2O_3(0001) Surface: Evidence for Domains of Distinct Chemistry. *Phys. Rev. Lett.* **1998**, *81*, 1038−1041.
(48) Bergermayer, W.; Schweiger, H.; Wimmer, E. *Ab Initio* Thermodynamics of Oxide Surfaces: O_2 on Fe_2O_3(0001). *Phys. Rev. B: Condens. Matter Mater. Phys.* **2004**, *69*, 195409.
(49) Yuan, L.; Van Der Geest, A. G.; Zhu, W.; Yin, Q.; Li, L.; Kolmogorov, A. N.; Zhou, G. Reduction of Cuo Nanowires Confined by a Nano Test Tube. *RSC Adv.* **2014**, *4*, 30259−30266.

DOI: 10.1021/acs.jpcc.6b02033
J. Phys. Chem. C 2016, 120, 14854−14862